

Article

High Pressure Induced Insulator-to-Semimetal Transition through Intersite Charge Transfer in $\text{NaMn}_7\text{O}_{12}$

Davide Delmonte ^{1,*}, Francesco Mezzadri ^{1,2} , Fabio Orlandi ³ , Gianluca Calestani ^{1,2},
Yehezkel Amiel ⁴ and Edmondo Gilioli ¹ 

¹ IMEM-CNR Parco Area delle Scienze 37/A, 43124 Parma, Italy; francesco.mezzadri@unipr.it (F.M.); gianluca.calestani@unipr.it (G.C.); edi@imem.cnr.it (E.G.)

² Department of Chemistry, Life Sciences and Environmental Sustainability, University of Parma, Parco Area delle Scienze 17/A, 43124 Parma, Italy

³ ISIS Facility, STFC Rutherford Appleton Laboratory, Oxon OX11 0QX, UK; fabio.orlandi@stfc.ac.uk

⁴ School of Physics and Astronomy, Tel-Aviv University, Tel-Aviv 69978, Israel; hezy.amiel@gmail.com

* Correspondence: davide.delmonte@imem.cnr.it

Received: 11 January 2018; Accepted: 31 January 2018; Published: 3 February 2018

Abstract: The pressure-dependent behaviour of $\text{NaMn}_7\text{O}_{12}$ (up to 40 GPa) is studied and discussed by means of single-crystal X-ray diffraction and resistance measurements carried out on powdered samples. A transition from thermally activated transport mechanism to semimetal takes place above 18 GPa, accompanied by a change in the compressibility of the system. On the other hand, the crystallographic determinations rule out a symmetry change to be at the origin of the transition, despite all the structural parameters pointing to a symmetrizing effect of pressure. Bond valence sum calculations indicate a charge transfer from the octahedrally coordinated manganese ions to the square planar ones, likely favouring the delocalization of the carriers.

Keywords: strongly correlated systems; high pressure; charge ordering; MIT

1. Introduction

Strongly correlated oxides can display a wide spectrum of intriguing properties, including magnetoresistance, half-metallicity, superconductivity, heavy fermion behaviour, and metal-insulator transition (MIT), with potential applications such as spintronics, superconductive devices or magnetoresistive memories. Often, different perturbations, like magnetic or electrical fields, temperature, doping or strain and pressure, can modify the material's electronic band structure [1]. Aside from the obvious structural variations (shortening of the bond distances, increased density, Jahn-Teller (JT) distortion), the application of external pressure to strongly correlated systems may lead to a wide range of phenomena, such as quenching of the orbital moment, spin crossover (high- to low-spin transition), metal-metal inter-valence charge transfer, MIT, etc. Mott insulators are likely to show metallization at high pressure due to competition between Coulomb repulsion and bandwidth. The latter is more susceptible to applied pressure [2], and therefore, experiments in which the bandwidth can be controlled with pressure represent an experimental proof for the existing theories on the behaviour of the strongly correlated electron systems, as reported in MnO [3], BaCoS_2 [4], Ba_2IrO_4 [5], Ca_2RuO_4 [6] and in the organic compound bis(ethylenedithio)tetrathiafulvalene [7]. Quite often, pressure-induced MIT is associated with symmetry changes, as for instance in SrTiO_3 [8] or BiNiO_3 [9,10], where the suppression of charge disproportionation involving the $\text{Bi}^{3+}/\text{Bi}^{5+}$ ions is reported to bring from a triclinic insulating phase to higher-symmetry metallic phase. A similar case is PbCrO_3 [11], where at ambient pressure, $\text{Cr}^{3+}/\text{Cr}^{6+}$ charge disproportionation occurs with the 6s-6p

hybridization of the Pb^{2+} orbitals with the oxygen 2p ones accounting for the insulating properties, while high pressure induces a single Cr^{4+} state which gives rise to the metallic phase. In some cases, however, isostructural MIT can take place when the crystallographic modifications induced by applied pressure modulate the structural features without symmetry breaking, as in the case of PrNiO_3 [12], metal osmium [13], FeAs [14] and VO_2 [15]. In WSe_2 , the MIT is caused by the anisotropic character of the compressibility, which induces a structural transition characterized by a sliding of the 2D layers [16]. In MoS_2 , similar phenomena are observed, but accompanied by a discontinuous change in the lattice parameters variation with pressure [17]. Other mechanisms may be at the origin of high temperature metallization, as in the case of LaMnO_3 , where the phenomenon is claimed to be caused in the paramagnetic phase by orbital splitting of the majority-spin e_g bands [18,19]. The effect of pressure on ordering phenomena is crucial, as in $\text{Pr}_{1-x}\text{Ca}_x\text{MnO}_3$ [20], where the suppression of charge order is identified as the origin of the MIT, while in $\text{Pr}_{0.6}\text{Ca}_{0.4}\text{Mn}_{0.96}\text{Al}_{0.04}\text{O}_3$ the quenching of JT distortion [21] is the driving force of metallization.

“Quadruple-perovskite” manganites, having general formula $A\text{Mn}_3\text{Mn}_4\text{O}_{12}$, exhibit strong electronic correlations [22]. These materials are characterized by A site cation ordering, where $\frac{3}{4}$ of the original perovskite A sites are occupied by Mn^{3+} ions in an uncommon square planar coordination (Figure 1), only stabilized by high-pressure/high-temperature (HP/HT) synthesis. The valence of the A ion tunes the $\text{Mn}^{3+}/\text{Mn}^{4+}$ ratio on the B site, determining the crystal symmetry based on the specific charge and orbital ordering, as reported for compounds with $A = \text{Na}$ [23], Ca [24], (Sr, Cd) [25], Pb [26], La [27,28], Bi [29,30], Y [31], and Pr [32]. The high electronic correlations, the significant lattice distortions, the full oxygen occupation (contrary to what usually happens in the conventional “simple” perovskites) and the chemical order (hetero-valent manganese atoms occupy different crystallographic sites), make this class of materials an intriguing playground for the study of possible instabilities induced by external stimuli on both the structural and physical properties.

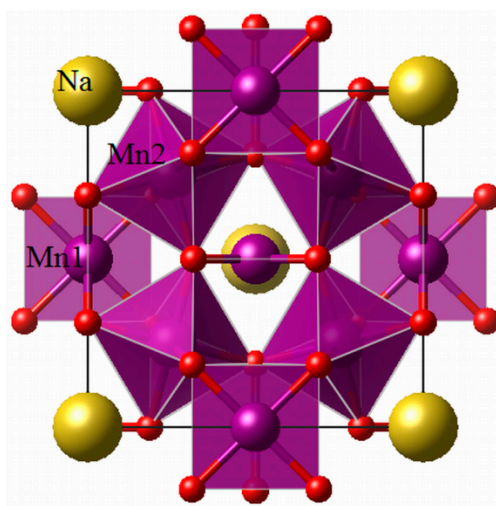


Figure 1. [100] projection of the quadruple perovskite structure having general formula $AA'_3B_4O_{12}$. In the present case, A , A' and B correspond to the Na1 , Mn1 and Mn2 sites, respectively.

The sodium-substituted quadruple-perovskite manganite, $\text{NaMn}_7\text{O}_{12}$ ($\text{NaMn}_3\text{Mn}_4\text{O}_{12}$), shows features that make it particularly interesting for pressure-dependent crystallographic and physical studies. The presence of Na^+ at the A site induces a 1:1 ratio of Mn^{3+} and Mn^{4+} on the B site. At room temperature, the symmetry is cubic ($Im\bar{3}$) as a consequence of the delocalization of the Mn^{3+} e_g electrons [33], while below 175 K, the JT effect leads to a complete charge and orbital ordering, giving rise to superlattice reflections with propagation vector $(1/2, 0, -1/2)$ observed by electron diffraction and powder synchrotron diffraction data [34]. The charge and orbital order scheme is then described by a monoclinic super-structure with $C2/m$ symmetry, which, in agreement with band structure

calculations [22], is characterized by a periodic scheme of JT apically elongated MnO_6 octahedra. The structural phase transition is accompanied by a change in both the resistivity and magnetic susceptibility and is clearly observed by diffraction techniques. The compound undergoes two different magnetic transitions at 125 K and 90 K related to the ordering of the Mn ions at the B and A' sites respectively. The weakly ferromagnetic transition observed below 125 K is related to spin canting of an E-type AFM structure with $(\frac{1}{2} 0 \frac{1}{2})$ propagation vector due to the large buckling of the MnO_6 octahedra. The 90 K transition is purely antiferromagnetic, and is ascribed to the ordering of the square planar Mn ions.

In the present work, the pressure dependent behaviour of $\text{NaMn}_7\text{O}_{12}$ is studied by means of single-crystal X-ray diffraction and resistance measurements up to about 40 GPa, showing the presence of an isostructural insulator-to-semimetal transition around 18 GPa, associated to an abrupt drop in the electrical resistance.

2. Experimental

$\text{NaMn}_7\text{O}_{12}$ samples were obtained by solid-state HP/HT reaction using a multi-anvil apparatus, as reported in Ref. [35]. The synthesis conditions were $P = 6.0$ GPa, $T = 830$ °C and reaction time 1 h. The $\text{NaMn}_7\text{O}_{12}$ crystals, having a typical size of 100 μm , were mechanically extracted by the bulk matrix. High-pressure electrical resistance measurements up to 40 GPa were performed on finely ground pure $\text{NaMn}_7\text{O}_{12}$ powder, with the van der Pauw method integrated in a Diamond Anvil Cell (DAC), using 300 μm culet anvils. A rhenium gasket was first filled with an insulator Al_2O_3 -NaCl mixture (3:1 atomic ratio), which also acts as a pressure medium. The crystalline samples were placed inside a 100 μm cavity drilled within the pressed insulating layer. Six platinum thin strips were used as electrical probes for resistance measurements, as shown in Figure 2; the measurements were carried out in all cases using 4 of the 6 contacts in the Van der Pauw mode, the two “additional” Pt strips were placed to have backup contacts in case of breaking, which quite often happens as the pressure is increased. The Pt contacts were connected to copper leads, at the base of the diamond anvil, using a silver epoxy. At each pressure, under both compression and decompression cycles, the sample resistance was measured by the standard four-probe method as a function of temperature in a cryostat.

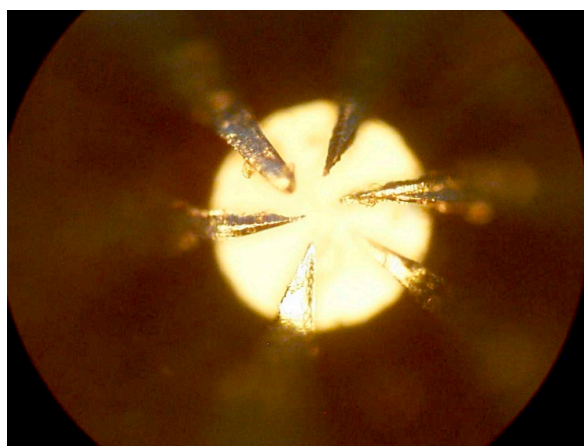


Figure 2. Diamond anvil cell's culet (300 μm diameter) with 6 Pt contacts.

Diffraction experiments were performed at the ID09 beam line of the ESRF (Grenoble, France) [36]. $\text{NaMn}_7\text{O}_{12}$ crystals were extracted from the HP/HT ceramic sample and introduced into a DAC with helium as a pressure medium to provide nearly hydrostatic conditions up to 40.8 GPa. For both resistivity and diffraction measurements, small rubies were inserted in the DAC, whose fluorescence was used as a pressure reference. The monochromatic X-ray radiation wavelength was set to $\lambda = 0.41456$ Å and diffraction data suitable for structure refinement were collected using a Mar555 flat

panel detector in the range $2.5^\circ < \theta < 19^\circ$ by 0.5° ω step in the angular interval $\pm 30^\circ$. The structure refinement was carried out by the SHELXL software (SheldrickGoettingen, Germany) [37], making use of anisotropic atomic displacements parameters (a.d.p.) for all atoms.

3. Results and Discussion

3.1. Transport Analysis

In the “low-pressure” regime ($P < 15$ GPa), the DAC in situ electrical measurements performed on $\text{NaMn}_7\text{O}_{12}$ are in agreement with previous observations [33]. Electrical resistance vs. T show a semiconductor-like thermal activated transport mechanism related to the manganese e_g electrons delocalized by kT energy (Figure 3a). By increasing pressure, a sharp resistance drop is observed above 18 GPa, yielding a semimetallic behaviour (Figure 3b), with almost temperature invariance of the resistance vs. temperature. By lowering T , no decreasing trend of resistance is detected up to the maximum value of the applied pressure, so that the high-pressure state of $\text{NaMn}_7\text{O}_{12}$ behaves like a semimetal rather than a conventional metal.

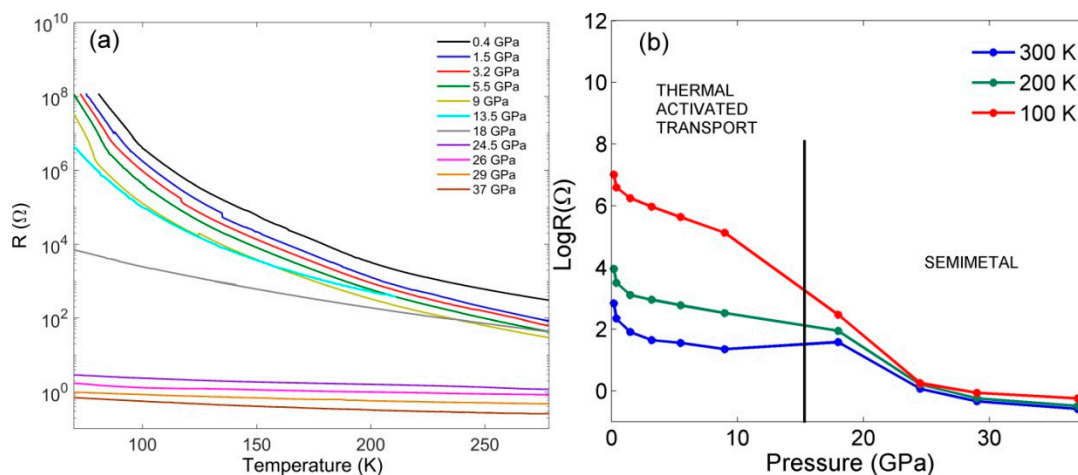


Figure 3. Electrical resistance vs. temperature of $\text{NaMn}_7\text{O}_{12}$ for different applied pressures (a) and electrical resistance vs. the applied pressure at different temperatures (b).

The Arrhenius plot derived from the R vs. T curves in the semiconducting regime shows the two critical temperatures of $\text{NaMn}_7\text{O}_{12}$, namely the charge ordering temperature $T_{\text{CO}} = 176$ K and the $T_{\text{N}} = 90$ K, distinguishable as deviations from the linear trend expected for a pure semiconductor, more evident at lower applied pressure (Figure 4). The E_{A} measured at the lowest reachable pressure (110 meV) is different from the value previously reported at ambient pressure (47 meV, [33]); measurements conducted on bulk pellets or ground powders are likely to give slightly different results, since the extrinsic phenomena and the occurrence of different percolative paths significantly affect the electrical transport mechanism. Moreover, the employed technique allows effective sample-wire contact only after the application of a (small) pressure; as a consequence, it was not possible to measure the electrical resistance below 0.4 GPa.

As the pressure increases, the charge-order transition anomaly becomes weaker and broader, in agreement with the symmetrizing effect of hydrostatic pressure, and is expected to finally lead to the melting of the charge and orbital orders. On the other hand, the anomaly observed at the T_{N} seems to move towards lower temperatures while getting more pronounced. By increasing pressure, the slope of the curves decreases, in accordance with the expected reduction of the thermally activated transport mechanism activation energy E_{A} , driven by the enhancement of the mechanical energy reducing the separation between the conduction and valence bands. Consequently, the E_{A} terms (obtained by the

linear fit of the Arrhenius curves in the intermediate regime $T_N < T < T_{CO}$ plotted vs. the applied pressure, shows a linear decrease from 110 to 87 meV (Figure 5).

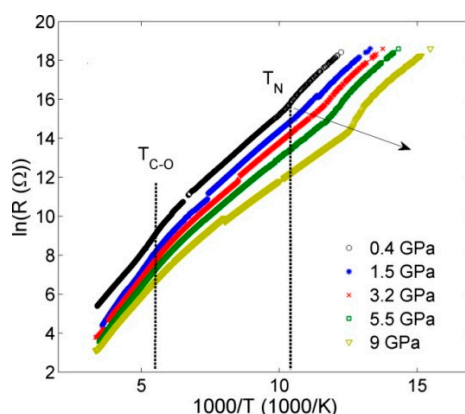


Figure 4. Arrhenius plot elaborated for the curves reported in Figure 2, limited to the thermal activated regime of $\text{NaMn}_7\text{O}_{12}$ ($P < 15$ GPa).

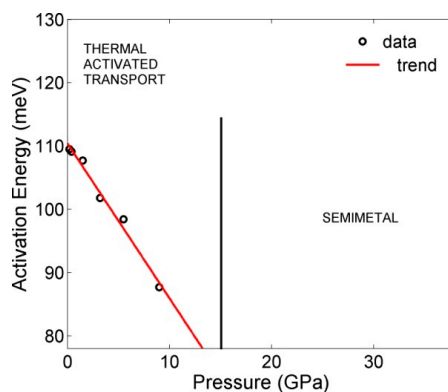


Figure 5. Calculated activation energy E_A vs. P in the “low pressure” thermal activated regime of $\text{NaMn}_7\text{O}_{12}$ ($P < 15$ GPa).

3.2. Structural Analysis

Single-crystal XRD experiments were carried out at room temperature in the 0.1–40.1 GPa range. Although the use of the DAC did not permit the collection of a significant portion of the Ewald sphere, the high symmetry of the analysed phase provides a sufficient number of equivalencies. The structure refined against the 0.3 GPa data is in excellent agreement with the previously reported crystallographic information: $Im\bar{3}$ symmetry (S.G. number 204), compatible with the absence of charge and orbital ordering [33]. The Na ion lies at the $2a$ site, while Mn1 and Mn2 are located at the $6b$ and $8c$ positions, respectively. Mn2 displays an octahedral coordination, while Mn1 a strongly distorted dodecahedral environment, often reported as square planar due to the large elongation of eight Mn–O bonds, four of which exceed 2.5 Å and four of which are above 3 Å (Figure 1).

It should be noted that all the atoms are located at high-symmetry positions with fixed x , y , z coordinates, except the sole oxygen atom, which is found at a low-symmetry site: $24g$ with $(0, y, z)$ coordinates.

While the $Im\bar{3}$ symmetry and the crystal structure are retained through the entire investigated pressure range, a very small change in the compressibility coefficient is detectable around the electrical transition, as shown in Figure 6. The refined lattice parameters, relevant bond distances and Mn–O–Mn

tilt angle are reported in Table 1. All the parameters show monotone variations in the investigated pressure range, with the cation-oxygen bond lengths decreasing with increasing pressure.

On the other hand, at about 18 GPa (matching the insulator to semimetal transition), the compressibility of the manganese-oxygen bond system abruptly decreases, with the Mn1 atom in square planar coordination displaying the most relevant variation (Figure 7).

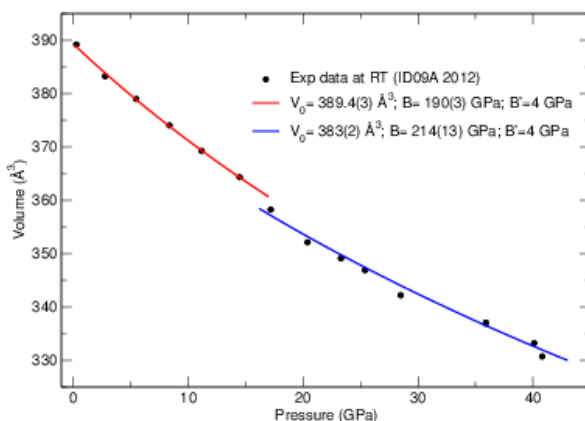


Figure 6. NaMn₇O₁₂ cell volume vs. pressure. Fittings were performed using the Birch–Murnaghan equation. B is the bulk modulus, and B' is set to 4. A change in the compressibility is observed at about 16 GPa. Error bars are smaller than the corresponding symbols.

Table 1. Lattice parameter, cell volume and selected bond lengths of NaMn₇O₁₂ at different applied pressures.

P (GPa)	a (Å)	V (Å ³)	Na1-O1 (Å)	Mn1-O1 (Å)	Mn1-O1 (Å)	Avg. Mn1-O1	Mn2-O1 (Å)	Mn2-O1-Mn2 (°)
0.3	7.301(2)	389.2(9)	2.644(7)	1.943(2)	2.6867(6)	2.3149(10)	1.916(7)	139.9(4)
2.8	7.264(2)	383.2(9)	2.629(4)	1.9320(15)	2.6734(6)	2.3027(8)	1.909(4)	140.1(2)
5.5	7.237(2)	379.0(9)	2.618(7)	1.924(3)	2.6648(6)	2.2944(15)	1.904(7)	140.2(4)
8.4	7.205(2)	374.0(9)	2.605(8)	1.918(3)	2.6610(12)	2.2895(16)	1.901(8)	140.3(4)
11.2	7.174(2)	369.3(9)	2.593(4)	1.9063(14)	2.6411(6)	2.2737(8)	1.891(4)	140.4(2)
14.5	7.142(2)	364.3(9)	2.582(3)	1.8974(11)	2.629(6)	2.263(3)	1.884(3)	140.45(16)
17.2	7.102(2)	358.3(9)	2.566(3)	1.8853(10)	2.6128(6)	2.2491(6)	1.878(3)	140.70(15)
20.4	7.062(2)	352.2(9)	2.546(4)	1.8745(13)	2.6042(6)	2.2394(7)	1.868(4)	140.7(2)
23.3	7.041(2)	349.1(9)	2.538(7)	1.867(2)	2.5932(6)	2.2301(10)	1.8682(7)	141.1(4)
25.4	7.026(2)	346.9(9)	2.534(4)	1.8637(14)	2.5881(6)	2.2259(8)	1.863(4)	142.0(2)
28.5	6.995(2)	342.3(9)	2.537(11)	1.857(10)	2.5606(6)	2.2088(6)	1.854(3)	141.2(6)
35.9	6.959(2)	333.2(9)	2.516(4)	1.8510(13)	2.5763(6)	2.2135(7)	1.859(4)	141.8(2)
40.1	6.933(2)	330.7(9)	2.490(6)	1.834(2)	2.5566(6)	2.1953(10)	1.853(6)	141.8(4)

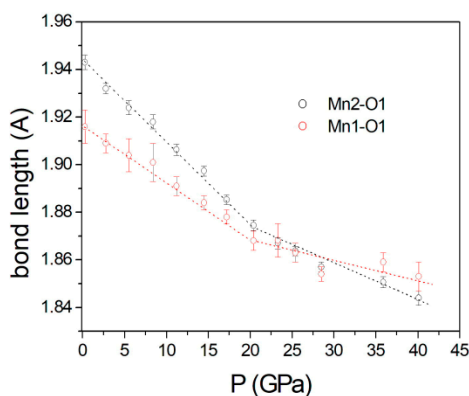


Figure 7. Pressure dependence of the manganese-oxygen bond lengths. A slope change is observed at 18 GPa, where the Mn1-O1 \cong Mn2-O1 bonds.

Interestingly, the Mn-O-Mn bond angles (Figure 8) retain a linear trend over the whole pressure range, showing an opposite slope for the octahedral tilt angle (Mn2-O1-Mn2), which increases with pressure, contrary to (Mn1-O1-Mn2). This behaviour is a consequence of the symmetrizing effect of pressure, which forces the framework towards the undistorted simple perovskite geometry, where the Mn2-O1-Mn2 and Mn1-O1-Mn2 are 180° and 90° , respectively. In order to qualitatively evaluate the valence variations on the two symmetry-independent manganese ions induced by pressure, bond valence sum (BVS) calculations were performed by using the refined crystal data [38]. To this end, the Mn-O bond distances were normalized following the formula: $d_{\text{norm}} = d_P \cdot a_{P0} / a_P$, where d_P is the bond distance at a chosen pressure, a_P is the lattice parameter at the same pressure and a_{P0} is the $\text{NaMn}_7\text{O}_{12}$ lattice parameter at room pressure. This operation is required to eliminate from the calculation the simple effects of the compressibility, since the reference bond length used in BVS is valid at room pressure.

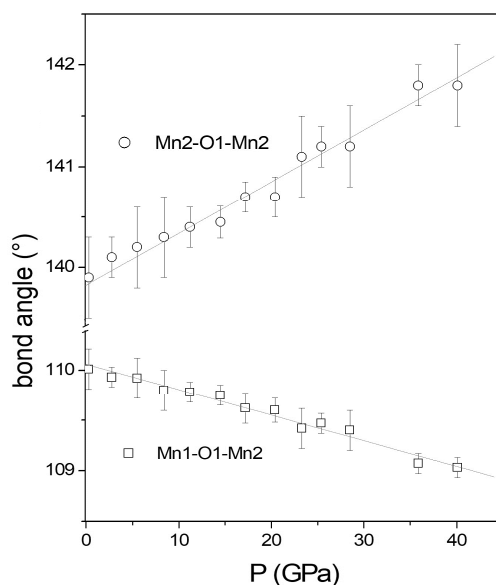


Figure 8. Mn-O-Mn bond angles in the 0–40 GPa pressure range. Mn2-O1-Mn2 monotonically evolves towards the 180° value, while Mn1-O1-Mn2 approaches 90° .

The obtained d_{norm} values and the corresponding valence of the manganese ions are reported in Figure 9. It should be noted that d_{norm} only depends on the oxygen atom displacement within the unit cell, given that the lattice parameter contribution to compressibility has been stripped out through normalization. Consequently, the linear trend displayed by the normalized values of Mn1-O1 and Mn2-O1 distances over the whole investigated pressure range, indicates that the anomaly previously observed in the refined bond length trends is directly related to the change in the lattice compressibility observed at the insulator-to-semimetal transition.

Moreover, the normalization procedure reveals a completely different behaviour for the Mn1 and Mn2 ions with respect to the unprocessed data. Indeed, the Mn-O bond distance in the square planar coordination increases by increasing the pressure, contrary to the octahedral site. The BVS values at the lowest reachable pressure (0.3 GPa), being 3.03 and 3.67 for the square planar and octahedral coordination, respectively, are quite close to the values expected by the nominal formula $\text{NaMn}^{\text{III}}_3(\text{Mn}^{\text{III}}_2\text{Mn}^{\text{IV}}_2)\text{O}_{12}$ (3 and 3.5). It is interesting to note that, when the average manganese valence is taken into account, the calculated value is not only in good agreement with the nominal one (3.29, given by 5 Mn^{3+} and 2 Mn^{4+} in the structure), but also remains practically constant, ranging from 3.39 to 3.36, over the whole pressure range. This indicates the substantial accuracy of the normalization applied to the bond distances and of the used model. On the other hand, it turns out that the system

experiences, with increasing pressure, a relevant charge transfer from the Mn2 to the Mn1 sites. The BVS of Mn2 undergoes a 3% increase from 3.67 to 3.78, whereas those of Mn1 decreases from 3.03 to 2.79 (8%), causing the observed decrease of the normalized volume of the MnO_6 octahedra accompanied by the elongation of the normalized square planar bonds (Figure 9). On the basis of these results, the increase in pressure progressively extends the delocalization, even to the A' site electrons, playing an important role in determining the electric transition. Similar phenomena are reported for $\text{LaCu}_3\text{Fe}_4\text{O}_{12}$ [39], where intersite charge transfer at room temperature occurs by applying pressure between the A-site Cu and B-site Fe, leading to a first-order transition from $\text{LaCu}^{3+}_3\text{Fe}^{3+}_4\text{O}_{12}$ (at low pressure) to $\text{LaCu}^{2+}_3\text{Fe}^{3.75+}_4\text{O}_{12}$ (high pressure). The transition is accompanied by a structural phase transition related to the different charge ordering scheme yielding significant reduction of unit-cell volume and a change from antiferromagnetic-insulating to paramagnetic-metallic state. No symmetry change is observed in the present case, being $\text{NaMn}_7\text{O}_{12}$ not charge and orbital ordered at ambient conditions. As a consequence, the role of pressure in modifying the electronic band structure cannot be ruled out, but the charge transfer between octahedral to square planar sites probably plays the central role in inducing the semimetallic behaviour at high pressures instead of the pure metallic character observed in $\text{LaCu}_3\text{Fe}_4\text{O}_{12}$.

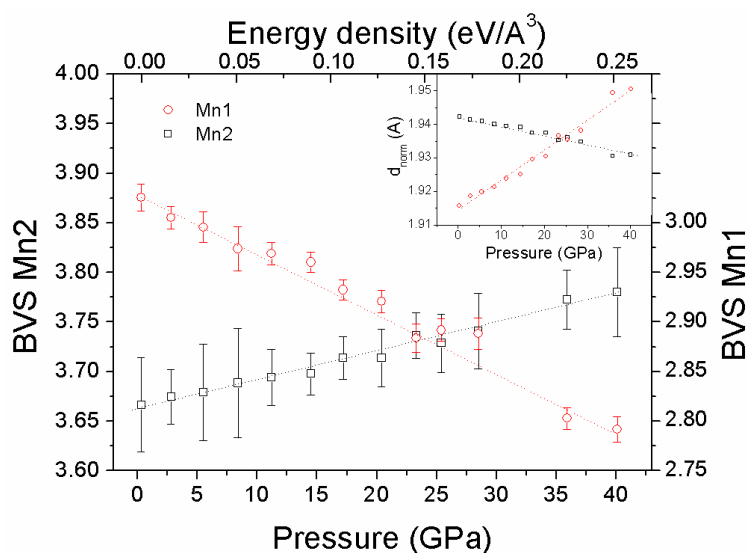


Figure 9. Bond Valence Sum and d_{norm} values (inset) as a function of pressure for the Mn1 and Mn2 atoms. The two sites display an opposite trend, pointing to an intersite charge transfer taking place from the octahedral to the square planar coordinated site.

4. Conclusions

The in situ, high-pressure powder electrical resistance measurements demonstrate that $\text{NaMn}_7\text{O}_{12}$, a metastable, charge-ordered manganite with quadruple-perovskite structure, undergoes an insulator-to-semimetal transition at about 18 GPa.

Across such transition, as refined by high-pressure single-crystal X-ray diffraction, $\text{NaMn}_7\text{O}_{12}$ retains the cubic ($Im\bar{3}$) structure with no symmetry breaking and non-relevant anomalies, or jump in the unit cell volume vs. P . On the contrary, charge transfer from the Mn2 (on the B site) to the Mn1 ions (on the A' site) is detected as the pressure increases, explaining the transformation of the system from an insulating to a semimetallic state. In this framework, the drop of the electric resistance can be interpreted as a significant electronic charge delocalization at the A' site favoured by the narrowing of the band gap.

Acknowledgments: The authors gratefully thank Andrea Prodi, Massimo Marezio, Andrea Gauzzi, Moshe Pasternak and Gregory Kh. Rozenberg for fruitful discussion. Edmondo Gilioli thanks the “SCENET exchange visits” program, funded by the NoE (Network of Excellence) SCENET (the European Network for Superconductivity, project No. BRRT CT98 5059). ESRF is acknowledged for provision of beamtime and Michael Hanfland and Marco Merlini for their assistance at the ID09A beamline.

Author Contributions: Edmondo Gilioli and Gianluca Calestani conceived the experiments; Yehezkel Amiel performed the DAC experiments; Davide Delmonte, Francesco Mezzadri, Fabio Orlandi, Gianluca Calestani and Edmondo Gilioli analyzed the data and contributed to the text; Davide Delmonte wrote, edited and submitted the paper.

Conflicts of Interest: The authors declare no conflict of interest.

References

1. Mizokawa, T. Metal-insulator transitions: Orbital control. *Nat. Phys.* **2013**, *9*, 612–613. [[CrossRef](#)]
2. Cui, C.; Tyson, T.A. Correlations between pressure and bandwidth effects in metal-insulator transitions in manganites. *Appl. Phys. Lett.* **2004**, *84*, 942–944. [[CrossRef](#)]
3. Yoo, C.S.; Maddox, B.; Klepeis, J.-H.P.; Iota, V.; Evans, W.; McMahan, A.; Hu, M.Y.; Chow, P.; Somayazulu, M.; Hausermann, D.; et al. First-Order isostructural mott transition in highly compressed MnO. *Phys. Rev. Lett.* **2005**, *94*, 115502. [[CrossRef](#)] [[PubMed](#)]
4. Yasui, Y.; Sasaki, H.; Sato, M.; Ohashi, M.; Sekine, Y.; Murayama, C.; Mōri, N. Studies of pressure-induced mott metal-insulator transition of BaCoS₂. *J. Phys. Soc. Jpn.* **1999**, *68*, 1313–1320. [[CrossRef](#)]
5. Orii, D.; Sakata, M.; Miyake, A.; Shimizu, K.; Okabe, H.; Isobe, M.; Takayama-Muromachi, E.; Akimitsu, J. Pressure-induced metal-insulator transition of the Mott insulator Ba₂IrO₄. *J. Korean Phys. Soc.* **2013**, *63*, 349–351. [[CrossRef](#)]
6. Nakamura, F.; Goko, T.; Ito, M.; Fujita, T.; Nakatsuji, S.; Fukazawa, H.; Maeno, Y.; Alireza, P.; Forsythe, D.; Julian, S.R. From Mott insulator to ferromagnetic metal: A pressure study of Ca₂RuO₄. *Phys. Rev. B* **2002**, *65*, 220402. [[CrossRef](#)]
7. Oike, H.; Miyagawa, K.; Taniguchi, H.; Kanoda, K. Pressure-Induced mott transition in an organic superconductor with a finite doping level. *Phys. Rev. Lett.* **2015**, *114*, 067002. [[CrossRef](#)] [[PubMed](#)]
8. Dai, L.D.; Wu, L.; Li, H.P.; Hu, H.Y.; Zhuang, Y.K.; Liu, K.X. Evidence of the pressure-induced conductivity switching of yttrium-doped SrTiO₃. *J. Phys. Condens. Matter* **2016**, *28*, 475501. [[CrossRef](#)] [[PubMed](#)]
9. Ishiwata, S.; Azuma, M.; Takano, M. Pressure-induced metal-insulator transition in BiNiO₃. *Solid State Ion.* **2004**, *172*, 569–571. [[CrossRef](#)]
10. Cai, M.Q.; Yang, G.W.; Tan, X.; Cao, Y.L.; Wang, L.L.; Hu, W.Y.; Wang, G. Vacancy-driven ferromagnetism in ferroelectric PbTiO₃. *Appl. Phys. Lett.* **2007**, *91*, 101901. [[CrossRef](#)]
11. Cheng, J.; Kweon, K.E.; Larregol, S.A.; Ding, Y.; Shirako, Y.; Marshall, L.G.; Li, Z.-Y.; Li, X.; dos Santos, A.M.; Suhomel, M.R.; et al. Charge disproportionation and the pressure-induced insulator-metal transition in cubic perovskite PbCrO₃. *Proc. Natl. Acad. Sci. USA* **2015**, *112*, 1670–1674. [[CrossRef](#)] [[PubMed](#)]
12. Medarde, M.; Mesot, J.; Lacorre, P.; Rosenkranz, S.; Fischer, P.; Gobrecht, K. High-pressure neutron-diffraction study of the metallization process in PrNiO₃. *Phys. Rev. B* **1995**, *52*, 9248. [[CrossRef](#)]
13. Occelli, F.; Farber, D.L.; Badro, J.; Aracne, C.M.; Teter, D.M.; Hanfland, M.; Canny, B.; Couzinet, B. Experimental evidence for a high-pressure isostructural phase transition in osmium. *Phys. Rev. Lett.* **2004**, *93*, 095502. [[CrossRef](#)] [[PubMed](#)]
14. Liu, Q.; Yu, X.; Wang, X.; Deng, Z.; Lv, Y.; Zhu, J.; Zhang, S.; Liu, H.; Yang, W.; Wang, L.; et al. Pressure-Induced isostructural phase transition and correlation of FeAs coordination with the superconducting properties of 111-Type Na_{1-x}FeAs. *J. Am. Chem. Soc.* **2011**, *133*, 7892–7896. [[CrossRef](#)] [[PubMed](#)]
15. Arcangeletti, E.; Baldassarre, L.; Di Castro, D.; Lupi, S.; Malavasi, L.; Marini, C.; Perucchi, A.; Postorino, P. Evidence of a pressure-induced metallization process in monoclinic VO₂. *Phys. Rev. Lett.* **2007**, *98*, 196406. [[CrossRef](#)] [[PubMed](#)]
16. Wang, X.; Chen, X.; Zhou, Y.; Park, C.; An, C.; Zhou, Y.; Zhang, R.; Gu, C.; Yang, W.; Yang, Z. Pressure-induced iso-structural phase transition and metallization in WSe₂. *Sci. Rep.* **2017**, *7*, 46694. [[CrossRef](#)] [[PubMed](#)]

17. Chi, Z.H.; Zhao, X.M.; Zhang, H.; Goncharov, A.F.; Lobanov, S.S.; Kagayama, T.; Sakata, M.; Chen, X.J. Pressure-induced metallization of molybdenum disulfide. *Phys. Rev. Lett.* **2014**, *113*, 036802. [[CrossRef](#)] [[PubMed](#)]
18. Fuhr, J.D.; Avignon, M.; Alascio, B. Pressure-Induced Insulator-Metal Transition in LaMnO₃: A Slave-Boson Approach. *Phys. Rev. Lett.* **2008**, *100*, 216402. [[CrossRef](#)] [[PubMed](#)]
19. Loa, I.; Adler, P.; Grzechnik, A.; Syassen, K.; Schwarz, U.; Hanfland, M.; Rozenberg, G.K.; Gorodetsky, P.; Pasternak, M.P. Pressure-Induced quenching of the jahn-teller distortion and insulator-to-metal transition in LaMnO₃. *Phys. Rev. Lett.* **2001**, *87*, 125501. [[CrossRef](#)] [[PubMed](#)]
20. Moritomo, Y.; Kuwahara, H.; Tomioka, Y. Pressure effects on charge-ordering transitions in perovskite manganites. *Phys. Rev. B* **1997**, *55*, 7549–7556. [[CrossRef](#)]
21. Arumugam, S.; Thiyagarajan, R.; Kalaiselvan, G.; Sivaprakash, P. Pressure induced insulator-metal transition and giant negative piezoresistance in Pr_{0.6}Ca_{0.4}Mn_{0.96}Al_{0.04}O₃ polycrystal. *J. Magn. Magn. Mater.* **2016**, *417*, 69–74. [[CrossRef](#)]
22. Streltsov, S.V.; Khomskii, D.I. Jahn-Teller distortion and charge, orbital, and magnetic order in NaMn₇O₁₂. *Phys. Rev. B* **2014**, *89*, 201115. [[CrossRef](#)]
23. Marezio, M.; Dernier, P.D.; Chenavas, J.; Joubert, J.C. High pressure synthesis and crystal structure of NaMn₇O₁₂. *J. Solid State Chem.* **1973**, *6*, 16–20. [[CrossRef](#)]
24. Bochu, B.; Buevoz, J.L.; Chenavas, J.; Collomb, A.; Joubert, J.C.; Marezio, M. Bond lengths in ‘CaMn₃’ (Mn₄)O₁₂: A new Jahn-Teller distortion of Mn³⁺ octahedra. *Solid State Commun.* **1980**, *36*, 133–138. [[CrossRef](#)]
25. Belik, A.; Glazkova, Y.K.; Katsuya, Y.; Tanaka, M.; Sobolev, A.V.; Presniakov, A. Low-Temperature structural modulations in CdMn₇O₁₂, CaMn₇O₁₂, SrMn₇O₁₂, and PbMn₇O₁₂ perovskites studied by synchrotron X-ray powder diffraction and mössbauer spectroscopy. *J. Phys. Chem. C* **2016**, *120*, 8278–8288. [[CrossRef](#)]
26. Locherer, T.; Dinnebier, R.; Kremer, R.K.; Greenblatt, M.; Jansen, M. Synthesis and properties of a new quadruple perovskite: A-site ordered PbMn₃Mn₄O₁₂. *J. Solid State Chem.* **2012**, *190*, 277–284. [[CrossRef](#)]
27. Prodi, A.; Gilioli, E.; Cabassi, R.; Bolzoni, F.; Licci, F.; Huang, Q.; Lynn, J.W.; Affronte, M.; Gauzzi, A.; Marezio, M. Magnetic structure of the high-density Single-Valent e_g Jahn-Teller system LaMn₇O₁₂. *Phys. Rev. B* **2009**, *79*, 085105. [[CrossRef](#)]
28. Liu, X.J.; Lv, S.H.; Pan, E.; Meng, J.; Albrecht, J.D. First-principles study of crystal structural stability and electronic and magnetic properties in LaMn₇O₁₂. *J. Phys. Condens. Matter* **2010**, *22*, 246001. [[CrossRef](#)] [[PubMed](#)]
29. Mezzadri, F.; Calestani, G.; Calicchio, M.; Gilioli, E.; Bolzoni, F.; Cabassi, R.; Marezio, M.; Migliori, A. Synthesis and characterization of multiferroic BiMn₇O₁₂. *Phys. Rev. B* **2009**, *79*, 100106. [[CrossRef](#)]
30. Mezzadri, F.; Buzzi, M.; Pernechele, C.; Calestani, G.; Solzi, M.; Migliori, A.; Gilioli, E. Polymorphism and Multiferroicity in Bi_{1-x/3}(Mn^{III})₃(Mn^{III}_{4-x}Mn^{IV}_x)O₁₂. *Chem. Mater.* **2011**, *23*, 3628–3635. [[CrossRef](#)]
31. Verseils, M.; Mezzadri, F.; Delmonte, D.; Baptiste, B.; Klein, Y.; Shcheka, S.; Chapon, L.C.; Hansen, T.; Gilioli, E.; Gauzzi, A. Effect of chemical pressure induced by La³⁺/Y³⁺ substitution on the magnetic ordering of (AMn₃)Mn₄O₁₂ quadruple perovskite. *Phys. Rev. Mater.* **2017**, *1*, 064407. [[CrossRef](#)]
32. Mezzadri, F.; Calicchio, M.; Gilioli, E.; Cabassi, R.; Bolzoni, F.; Calestani, G.; Bissoli, F. High-pressure synthesis and characterization of PrMn₇O₁₂ polymorphs. *Phys. Rev. B* **2009**, *79*, 014420. [[CrossRef](#)]
33. Prodi, A.; Gilioli, E.; Gauzzi, A.; Licci, F.; Marezio, M.; Bolzoni, F.; Huang, Q.; Santoro, A.; Lynn, J. Charge, orbital and spin ordering phenomena in the mixed valence manganite (NaMn³⁺)₃(Mn³⁺₂Mn⁴⁺₂)O₁₂. *Nat. Mater.* **2004**, *3*, 48–52.
34. Prodi, A.; Daoud-Aladine, A.; Gozzo, F.; Schmitt, B.; Lebedev, O.; van Tendeloo, G.; Gilioli, E.; Bolzoni, F.; Aruga-Katori, H.; Takagi, H.; et al. Commensurate structural modulation in the charge- and orbitally ordered phase of the quadruple perovskite (NaMn₃)Mn₄O₁₂. *Phys. Rev. B* **2014**, *90*, 180101. [[CrossRef](#)]
35. Gilioli, E.; Calestani, G.; Licci, F.; Gauzzi, A.; Bolzoni, F.; Prodi, A.; Marezio, M. P–T phase diagram and single crystal structural refinement of NaMn₇O₁₂. *Solid State Sci.* **2005**, *7*, 746–752. [[CrossRef](#)]
36. Merlini, M.; Hanfland, M. Single-crystal diffraction at megabar conditions by synchrotron radiation. *High Press. Res.* **2013**, *33*, 511–522. [[CrossRef](#)]
37. Sheldrick, G.M. Crystal structure refinement with SHELXL. *Acta Crystallogr. C* **2015**, *71*, 3–8. [[CrossRef](#)] [[PubMed](#)]

38. Brown, I.D.; Altermatt, D. Bond-valence parameters obtained from a systematic analysis of the Inorganic Crystal Structure Database. *Acta Crystallogr. B* **1985**, *41*, 244–247. [[CrossRef](#)]
39. Long, Y.; Kawakami, T.; Chen, W.; Saito, T.; Watanuk, T.; Nakakura, Y.; Liu, Q.; Jin, C.; Shimakawa, Y. Pressure effect on intersite charge transfer in a-site-ordered double-perovskite-structure oxide. *Chem. Mater.* **2012**, *24*, 2235–2239. [[CrossRef](#)]



© 2018 by the authors. Licensee MDPI, Basel, Switzerland. This article is an open access article distributed under the terms and conditions of the Creative Commons Attribution (CC BY) license (<http://creativecommons.org/licenses/by/4.0/>).